

Experimental characterization of vibrated granular rings

Z. A. Daya^{1,2}, E. Ben-Naim^{1,3} & R. E. Ecke^{1,2,3}

¹Center for Nonlinear Studies, ²Condensed Matter & Thermal Physics Group,

³Theoretical Division, Los Alamos National Laboratory, Los Alamos, NM 87545

(Dated: March 22, 2006)

We report an experimental study of the statistical properties of vibrated granular rings. In this system, a linked rod and bead metallic chain in the form of a ring is collisionally excited by a vertically oscillating plate. The dynamics are driven primarily by inelastic bead-plate collisions and are simultaneously constrained by the rings' physical connectedness. By imaging many instances of the ring configurations, we measure the ensemble averages and distributions of several physical characteristics on the scale of individual beads and composite ring. We study local properties such as inter-bead separation and inter-bonds angles, and global properties such as the radius of gyration and center of mass motion. We characterize scaling with respect to the size of the chain.

PACS numbers: 05.40.a, 81.05.Rm, 82.35.Lr

I. INTRODUCTION

In the last decade the study of granular materials has become a mainstream pursuit amongst physicists who have summarized the advances in recent reviews [1–3]. The broad spectrum of static and dynamic behaviors of granular media are being studied by a combination of state-of-the-art experiments, computer simulations and theoretical approaches. Shaken granular materials are one example of a comprehensively studied subset of this spectrum. Experiments and simulations on shaken grains have demonstrated a variety of phenomena such as localized structures [4], extensive patterns [5, 6], clustering [7, 8], compaction [9, 10] and non-Maxwellian statistics [11, 12].

Granular chains consist of hollow spheres connected by rods, *i.e.*, grains constrained by a chain backbone. In granular chains we get the juxtaposition of the hard grains of granular physics with the flexibility of polymers. The chains can be excited, say, by collisions with a vibrating plate and can be observed visually. As such they afford a simple system for the direct measurements of micro- and macro-scopic variables. Experiments on granular chains, supported by theoretical models and simulations, have probed the diffusive relaxation of a simply knotted chain [13], the dynamical behavior of a vertically excited hanging chain [14], the entropic tightening of a once-twisted “figure-8” ring [15] and the spontaneous formation of spirals [16].

In this paper we report our study of vibrated granular rings. Our experimental system consists of a vertically oscillated plate on which we place a granular ring constructed from a ball chain; a schematic is shown in Fig. 1. Rings are constructed by joining the two free ends of a chain. A chain with free ends suffers unequal excitation along its length since beads near the ends are less constrained and thus preferentially excited. Rings, which are devoid of free ends, restore the equality in excitation amongst the beads, and it is for this reason that they are particularly attractive to study.

In our experiments we control the amplitude and fre-

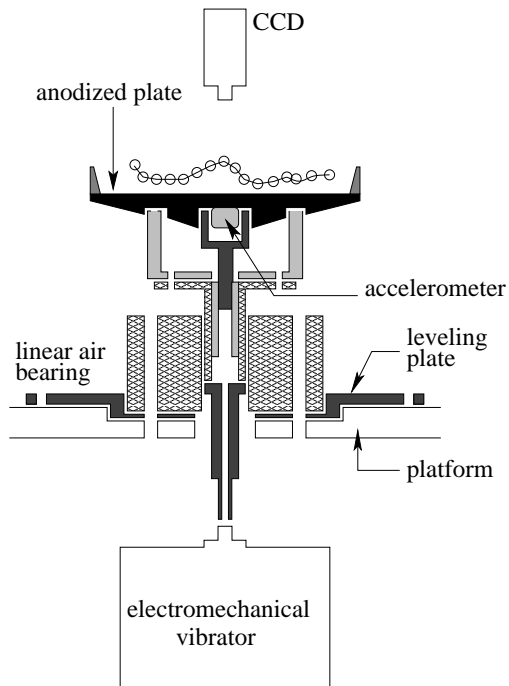


FIG. 1: A schematic of our experimental apparatus.

quency of the harmonically oscillated plate. A chain initially resting on the plate becomes airborne when the plate imparts to it an acceleration that exceeds the gravitational acceleration. Thereafter, collisions between the plate and chain appear to randomize the motion and shape of the granular ring. The collisions of different parts of the chain are asynchronous with the phase of the plate's oscillation. Further collisions amongst the beads on the chain occur frequently.

We observe the ring from above at a random phase of the oscillation. We acquire images which are two-dimensional projections of the position of the ring. From these images we obtain the spatial coordinates and order of the beads in the ring. Since the images are sequential and time stamped, we are also able to calculate differ-

ences and therefore dynamics. We make a large number of position measurements for rings under vertical vibration. From this data we study the geometrical properties on the bead scale, *i.e.*, local characteristics, and on the scale of the chain, *i.e.*, global characteristics. The local properties include the inter-bead separations, the bending angle between two consecutive rods, the average curvature and the dynamics of the beads. For the global characteristics we focus on descriptors of the size and overall motion of the ring. These are the radius of gyration and the dynamics of the rings' center of mass.

This paper is organized as follows. In Section II we describe the experimental apparatus, the specific design considerations, the image acquisition and analysis procedure. Our experimental results depend at most on the ordered positions of the beads in a ring and on the data acquisition rate. We have divided the results into local and global properties which are discussed in Sections III and IV respectively. Local (global) properties are relevant to the scale of the bead (ring). We discuss the inter-bead separation, the inter-rod angle, the average curvature and the bead dynamics as local properties. For global characteristics we discuss the radius of gyration and the average motion of the ring center of mass. A conclusion and an outline of future directions follows in Section V.

II. EXPERIMENT

In this Section we describe our experimental apparatus and our data extraction procedure. In overall design, the apparatus is comprised of an electromechanical shaker that drives a plate which is observed by a CCD camera. A schematic of our experimental setup is shown in Fig. 1.

A. The electromechanical vibration assembly

A commercial electromechanical shaker driven by a sinusoidal voltage input is used to oscillate a plate. The shaker operates electromagnetically with the current-carrying coil armature oscillating in the strong magnetic field of permanent ceramic magnets. The electromechanical shaker is coupled to the plate by a shaft but is otherwise vibrationally isolated from the rest of the apparatus. A massive aluminum platform that is rigidly bolted to the laboratory floor acts as a low-pass filter of vibrational noise. The shaft is guided by the bore of a precise square-section linear air bearing. In addition to linear motion, the square-section shaft decouples the plate from the rotational torque in the drive. The driving is thus accurately uni-axial and a leveling plate facilitates alignment with gravity. The shaft is coupled to the plate by two concentric cylindrical tubes. A sensitive accelerometer is attached centrally on the underside of the plate.

The plate is driven harmonically with amplitude A and angular velocity $\omega = 2\pi f$, where f is the driving fre-

quency. The dimensionless peak acceleration $\Gamma = A\omega^2/g$, where g is the gravitational acceleration, and the frequency f specify the driving conditions for the experiment. The shaker is operated at $f = 16$ Hz and $\Gamma = 2.12$ for all the experiments described in this paper. The shaker is protected from bearing the combined weight of the plate and shaft by adjustable counter-weighting springs such that the drive oscillates about its natural equilibrium position.

B. The plate and the granular rings

The plate is circular with a diameter of 11.50 inches and is made of stress-relieved aluminum. The primary design requirements are light weight, flexural stiffness and surface hardness. Aluminum's low density and comparable flexural properties to most metals make it a suitable choice. On oscillation we expect that bending modes of the plate are excited. The higher the stiffness the higher the frequencies excited. Since our experiments have drive frequency $f \sim 10$ Hz, we designed the plate so that its excitable bending modes had much higher frequencies. This is accomplished by tapering the lower surface of the plate and by boring out cylinders from this surface in a space-filling azimuthally symmetric manner. The cylinders bored out of the aluminum have various depths and diameters. The plate is at its thickest 1.50 inches decreasing to 0.25 inches at the boundary. These considerations lead to a selective damping of pure modes of the shaken plate. A further safeguard against exciting modes of the plate is achieved by forcing the plate at two annular regions rather than at the center or at the edge. The annular regions are at radial locations $1.25 \leq r \leq 2.00$ and $4.88 \leq r \leq 6.00$ inches. Surface hardness needed to withstand the many metal on metal collisions of the chains hitting the plate is attained by hard black anodization of the aluminum plate.

The granular chains are commercially available ball chains. They consist of hollow, approximately-spherical shells that are connected by dumb-bell shaped rods. We use two types of ball chains in our experiments. The smaller is made from nickel-plated stainless steel rods and beads. The beads have a nominal diameter of $\frac{3}{32}$ inches. The larger is a $\frac{1}{8}$ inch diameter brass chain. Thus there are typically 100 beads across the plate diameter. The chains are connected end to end to make rings. The splicing together of the free ends is natural in the sense that a rod from one of the end beads is inserted into the shell of the other end bead. The joined free ends could seldom be identified in the constructed ring. The tightest rings that we could make have 8 beads. Hence the angle θ between two consecutive rods is constrained so that $0 \leq \theta \leq 50^\circ$. Our experiments use rings with N beads where $13 \leq N \leq 309$. The rings are laterally confined to the plate by an acrylic boundary.

C. Data extraction

Our data consist of digital images of the granular ring on the plate. We illuminate the chain using approximately normally-incident light from far above the plate. To minimize reflection from the background, we paint the acrylic boundary black. Additionally, before black-anodizing the flat surface of the plate is roughened by sand blasting. The very shallow surface inhomogeneity helps randomize even simple collisions with the plate and diffusively scatters far-field light. The poorly reflective background reduces noise in the digital image. The normal far-field illumination gives an almost uniform reflected light intensity across the plate area. Furthermore, the light reflected by the beads is primarily from the center of the beads. Non-normal lighting preferentially illuminates crescent-shaped areas on the surface of the beads. A representative raw image is shown in Fig. 2a.

Typically, our images are acquired at sampling rates of 0.25 – 16 Hz and have a resolution of approximately 1000×1000 pixels. Depending on the data set we have between 8.8 and 13.0 pixels to the bead diameter d . The reflected light is brightest from the center of the beads and diminishes radially outwards. A sequence of standard image analysis procedures such as background subtraction, intensity rescaling, high-pass thresholding and smoothing result in reducing the data into roughly $N \times 7 \times 7$ non-zero pixels for N beads. Local maxima in the intensity field are then determined and ranked by their peak intensity. The intensity field of each set of 5×5 pixels centered about a local maximum is fit to an azimuthally symmetric Gaussian. The fit parameters of the position of the Gaussian peak are taken as the sub-pixel coordinates of the bead. The fit to the standard deviation of the Gaussian gives an estimate to the positional accuracy of about 0.05 bead diameters. Figure 2c shows a blow up of part of the raw image in Fig. 2a and our determination of the bead centers.

In most of the images, our data extraction procedure resulted in more than N local maxima. Most of these occur when a rod appears brighter than a bead. A rod between two beads is visible in Fig. 2c. The frequency of this occurrence is about 1% of the number of beads. Since the distance between the position of a rod and an adjacent bead is smaller than the minimum distance between two adjacent balls, we eliminated these by iteratively applying a strict minimum distance criterion.

The next step is to order the N coordinates so that the ring can be reconstructed. The ordering algorithm uses the geometrical restrictions imposed by the interconnecting rods. Given two adjacent beads, the third is searched for in the sector defined by the maximum inter-bead separation and angle. This efficient greedy algorithm requires N^2 operations to order an N bead chain. The overall accuracy of our data extraction process exceeds 96% *i.e.*, in less than 4% of the images are we unable to reconstruct the chain. There are various reasons for this. The beads are constructed by crimping sheet metal and

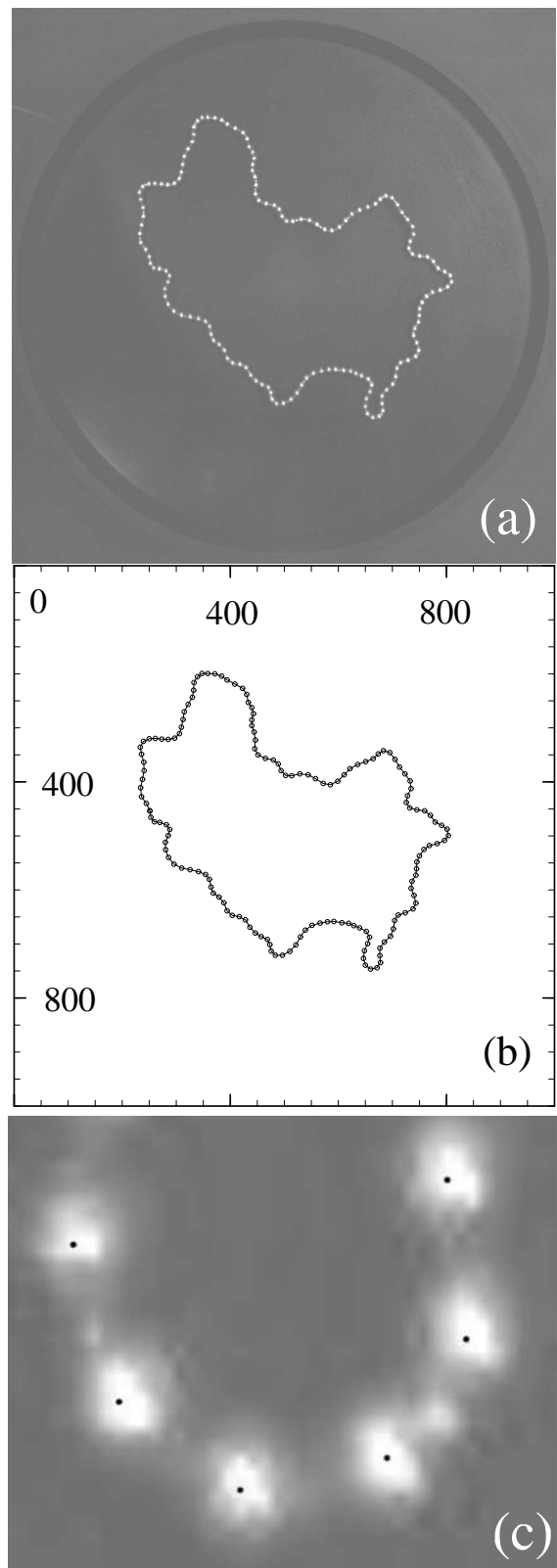


FIG. 2: (a) Raw data image, (b) reconstruction by identifying the bead coordinates (in pixels) and order, and (c) overlay of a section of the raw image and the position data (\bullet) for the center of the beads. Locally bright regions between beads in (c) correspond to reflection from an interconnecting rod.

so have a seam running along one half of a great circle. The seam is comparatively duller in reflected light than any other part of the beads and so in a few images our extraction process misses these beads. Since the images are two-dimensional projections of the chain, the strict inter-bead distance criteria can appear to be violated. In these cases our algorithms may allow a false bead position. In Fig. 2b, we show a complete reconstruction of a chain from the raw image data in Fig. 2a. Given the small number of misidentifications, we are confident that these issues have a small effect on the results reported below.

III. LOCAL PROPERTIES

In this Section we present our results on the local properties of vertically vibrated granular rings. Local properties are relevant to the scale of the bead and here we discuss the inter-bead separation, the inter-rod angle, the average curvature and the bead dynamics. We noted earlier that the chains are constructed out of hollow shells that are connected by rods. This connection imposes constraints on the minimum and maximum separation between beads, on the maximum bending that 3 adjacent beads can sustain, and on the displacements that occur on excitation.

A. Inter-bead separations

The inter-bead separation $\delta = |\mathbf{r}_{i+1} - \mathbf{r}_i|$ is measured between every two consecutive bead positions for brass and nickel rings. \mathbf{r}_i is position of bead i in two dimensions. Hence, there are N measurements of δ for an N -bead ring. Our data is based on no fewer than 5200 measurements of δ for $N = 13$ and more than 10^5 samples for $N \geq 256$. From these data, we construct the probability distribution function of the inter-bead separations $P(\delta)$.

In Fig. 3, we plot the mean $\langle \delta \rangle$ and standard deviation σ_δ as a function of N . For N sufficiently large, $\langle \delta \rangle$ and σ_δ are independent of N . The distributions $P(\delta)$ are similar in gross feature for the brass and nickel rings for the various lengths N . Combining the data for $30 \leq N \leq 309$, we obtain the distribution function shown in Fig. 4. The distribution has a sharp cut-off at $\delta \approx 1.4$ corresponding to the maximal extension between the beads. A much softer small δ cut-off appears at $\delta \approx 0.8$. The minimal distance in an accurately two-dimensional chain would be at $\delta = 1$. The quasi-two-dimensional motion of the chain and our measuring the motion on a planar projection allows values of $\delta < 1$. The peak of the distribution at small separations is possibly due to bead-bead frictional effects. Between the small- δ peak and the upper- δ cut-off we find that the distribution is roughly flat. These intermediate separations occur with significant and approximately equal probability, perhaps because of the constant rod-bead friction at these extensions.

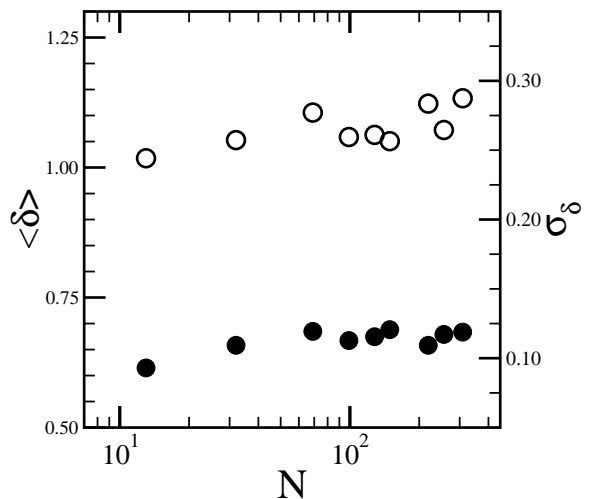


FIG. inter-

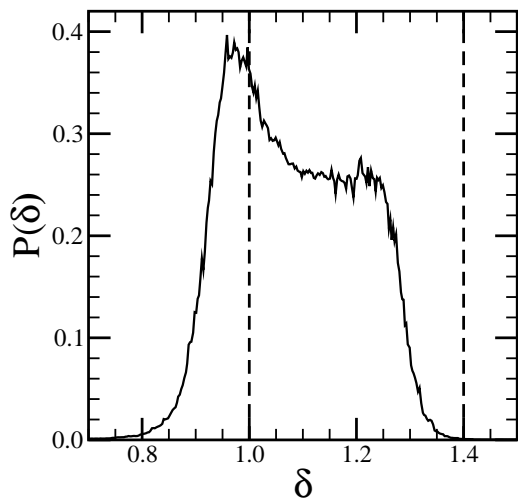


FIG. 4: The probability distribution $P(\delta)$ for the inter-bead separations. The distribution combines data for rings with lengths $30 \leq N \leq 309$. The dashed line $\delta = 1(1.4)$ in the theoretical lower (upper) bound.

B. Bending angles

Given the positional ordering $\mathbf{r}_{i-1}, \mathbf{r}_i, \mathbf{r}_{i+1}$ of three consecutive beads in the ring, we describe the bending by

$$\cos \theta = \frac{d\mathbf{r}_{i-1} \cdot d\mathbf{r}_i}{|d\mathbf{r}_{i-1}| |d\mathbf{r}_i|}, \quad (1)$$

where $d\mathbf{r}_i = \mathbf{r}_{i+1} - \mathbf{r}_i$. There are N values of $\cos \theta$ for every N -bead ring. As with the inter-bead separations, we have approximately 5200 measurements of $\cos \theta$ for $N = 13$ and more than 10^5 samples for $N \geq 256$ from which we determine the distribution function. In Fig. 5, we plot the mean $\langle \cos \theta \rangle$ and standard deviation $\sigma_{\cos \theta}$ of the bending distribution functions for granular rings as a function of N . As N increases, $\langle \cos \theta \rangle \rightarrow 1$ and

$\sigma_{\cos\theta} \rightarrow 0$. This large N behavior implies that a long ring is primarily composed of locally straight segments. For N approaching the smallest ring size of 8 beads, $\langle \cos\theta \rangle \rightarrow 0.7$ consistent with the tightest bending.

The large N limiting behavior of the mean bending angle is particularly interesting. In Fig. 6, we plot the difference between the limiting value of unity and the measured $\langle \cos\theta \rangle$. For an ideal circular ring with N beads, $1 - \langle \cos\theta \rangle \sim N^{-2}$. We find that although the granular ring becomes locally straight as its length increases, it does so very differently from a circular ring. Our data show a gentler approach with

$$1 - \langle \cos\theta \rangle \sim N^{-0.6}. \quad (2)$$

This implies that the chain curvature decreases slowly as the chain length increases.

The bending distributions for representative small and large rings are shown in Fig. 7. The distributions peak near $\cos\theta \sim 1$ and monotonically decrease for smaller $\cos\theta$. The peak and range depends weakly on the number of beads N . The peak probability for bending angles is higher for the longer rings whereas the range of bending angles is larger for the shorter chains. There are significant quantitative differences (not shown) between the distributions for brass and nickel rings but the qualitative features are similar. The principal difference is at large angles where the greater flexibility of the brass chains increases the range of variation in $\cos\theta$.

C. Average curvature

The vibrated rings sample many microscopic configurations subject only to the stretching and bending constraint

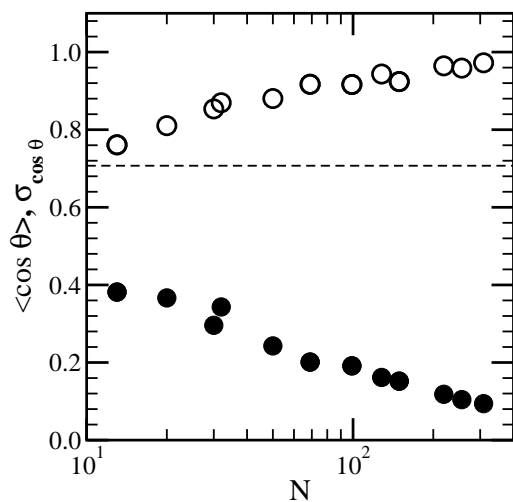


FIG. 5: The mean $\langle \cos\theta \rangle$ (\circ) and standard deviation $\sigma_{\cos\theta}$ (\bullet) of the bending angle $\cos\theta$ vs ring length N . The dashed line corresponds to the lower bound set for $\langle \cos\theta \rangle$ by a ring with $N = 8$.

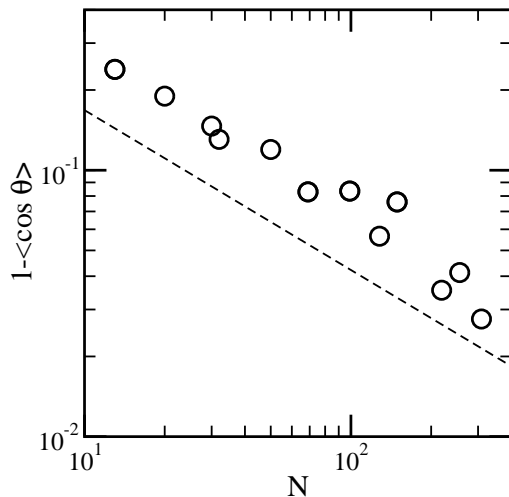


FIG. 6: Plot of $1 - \langle \cos\theta \rangle$ vs N . The dashed line is, up to a constant, $N^{-0.6}$

tual self-exclusion. One of the properties of the configuration is the overall extent to which the ring is curved. To probe this feature we use the ordered positions to compute the average squared curvature K which we define as

$$K = \frac{\oint \mathbf{k}(s) \cdot \mathbf{k}(s) ds}{\oint \mathbf{k}_{\text{circle}}(s) \cdot \mathbf{k}_{\text{circle}}(s) ds}, \quad (3)$$

where \mathbf{k} is given by

$$\mathbf{k}(s) = \frac{d^2\mathbf{r}}{ds^2}; \quad \mathbf{r}(s) = (x(s), y(s)). \quad (4)$$

In Eq. 4, s is the arc length along the chain and $\mathbf{r}(s)$ is a unit-speed reparametrization of the chain. Then, by definition $|d\mathbf{r}/ds| \equiv 1$ so $\mathbf{k}(s)$ measures the way

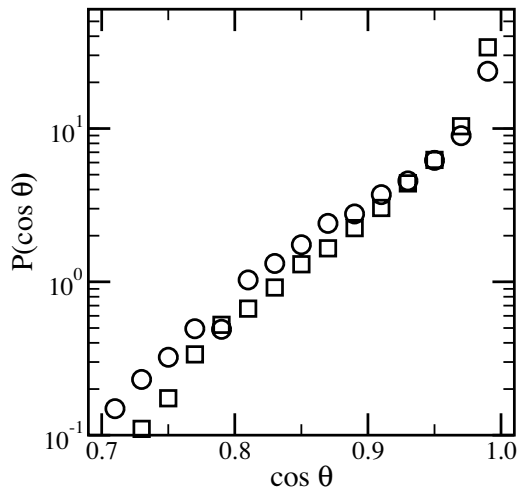


FIG. 7: The probability distribution of the bending angle $P(\cos\theta)$ for rings with lengths $N = 32$ (\circ) and $N = 128$ (\square).

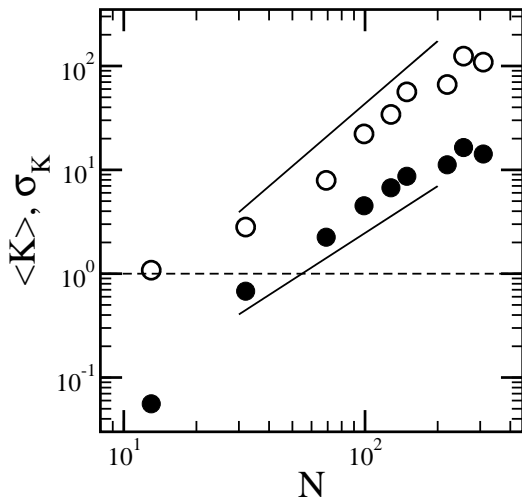


FIG. 8: The mean $\langle K \rangle$ (\circ) and standard deviation σ_K (\bullet) of the squared curvature, K vs ring length N . The horizontal dashed line $K = 1$ represents a circle. The solid lines are proportional to $N^{1.5}$ and N^2 .

the chain turns. $\mathbf{k}_{\text{circle}}(s)$ is obtained by computing Eq. 4 for a circle with circumference equal to the arc length of the chain. The local squared curvature is $k(s) = \mathbf{k}(s) \cdot \mathbf{k}(s)$. Averaging over the ring we get $\oint k(s) ds / \oint ds$. Similarly for the circle with circumference equal to the chain's length, we have an average squared curvature $\oint k_{\text{circle}}(s) ds / \oint ds$. Normalizing the average squared curvature of the ring by that of an equal arc length circle, we get the quantity K defined in Eq. 3.

As a procedure, for each ring, we first calculate its circumference by adding the separations between adjacent beads. We then reparameterize the positions of the beads by the arc length s so that $\mathbf{r}_i = (x_i, y_i) = (x(s_i), y(s_i))$ such that the ring has unit circumference and is traversed with unit speed. Since $\oint \mathbf{k}_{\text{circle}}(s) \cdot \mathbf{k}_{\text{circle}}(s) ds = 4\pi^2$ for a circle of unit length and speed, we have normalized K such that as the ring approaches a circle $K \rightarrow 1$. Hence K measures the departure from a circular shape. In practice, the integral in Eq. 3 is replaced by a summation over the N discrete bead positions and $\mathbf{k}(s_i)$ is approximated by the difference

$$\mathbf{k}(s_i) = \frac{d^2 \mathbf{r}_i}{ds_i^2} = \frac{d\mathbf{r}_{i+1} - d\mathbf{r}_i}{\frac{1}{2}(s_{i+1} - s_i) + \frac{1}{2}(s_i - s_{i-1})}. \quad (5)$$

Using in excess of 6800 images or approximately 425 realizations per chain, we have measured the mean and rms values of K for brass and nickel rings for several N . In Fig. 8, we plot the mean $\langle K \rangle$ and standard deviation σ_K as a function of N . The two smallest rings have $N = 13$ and 20 . They are approximately circular and tightly constrained, resulting in $\langle K \rangle \approx 1$; the smallest ring has $N = 8$ and is practically rigid. For larger N we find that the scaling exponent $\mu \sim 2$ in the power-law $\langle K \rangle \sim N^\mu$ for $20 \leq N \leq 256$. This implies, in agreement with Eq. 2, that as N increases, the ring increasingly

deviates from a circle. The standard deviation σ_K from the data shows a scaling relation $\sigma_K \sim N^\lambda$ with $\lambda \sim 1.5$. This observation is consistent with Eq. 2.

D. Bead displacements

The dynamics of the beads are studied by measuring the displacement of a bead as a function of time. It is well known that the mean square displacement of a randomly excited particle scales linearly with time while ballistic motion results in quadratic scaling. It is interesting to probe how a bead constrained to the ring behaves.

We restrict our analysis to images acquired at 16 Hz which is sufficiently fast so that bead positions between two consecutive images show small changes. Consequently, we can identify beads in an image with the preceding image. Discerning the bead identity is increasingly more difficult with slower image acquisition rates since the bead displacements are quite large. The ordered position data of the beads in the ring is obtained as described earlier in Section II C. Then assuming the bead identity in the first image, we order the bead positions of the second image so that they correspond to the preceding image. Since there is only 1 plate oscillation and therefore on average 1 chain excitation between consecutive images, we are confident that we have accurately identified the beads. Additionally, we visually verify the ordering for a subset of the data sets. We implement our bead identity algorithm by translating the data from both images to a common center of mass and then minimizing the mean square position difference between the two images up to cyclic permutations and orientation of the second image. The procedure is iterated until all the images are properly ordered.

The squared displacement that bead i in a ring with N beads undergoes between time τ and $\tau + t$ is $\Delta r_i^2(t, \tau, N) = (\mathbf{r}_i(\tau + t) - \mathbf{r}_i(\tau)) \cdot (\mathbf{r}_i(\tau + t) - \mathbf{r}_i(\tau))$. For the data, the times τ and t are chosen to coincide with the image acquisitions, *i.e.*, multiples of $1/16$ s, and the displacement is measured in units of the bead diameter. Note that both images are translated to the origin, *i.e.*, the center of mass is subtracted from the bead coordinates before calculating the squared displacement.

Averaging over all beads i in the ring and over possible values of τ , we define the mean squared bead displacement:

$$\langle \Delta r^2 \rangle(t, N) = \langle \Delta r_i^2(t, \tau, N) \rangle_{\tau, i}. \quad (6)$$

We probe the time dependence of $\langle \Delta r^2 \rangle$ by assuming a length dependent constant factor $\beta(N)$ such that the mean squared displacements are the same for the shortest experimentally observed time $t = 1/16$ s. In Fig. 9, we plot $\langle \Delta r^2 \rangle / \beta(N)$ versus t . For times corresponding to about 10 plate oscillations, $\langle \Delta r^2 \rangle / \beta(N)$ increases linearly with time for all rings. This behaviour is consistent with diffusive motion. Thus, although the ring is mechanically and athermally driven, collective properties may

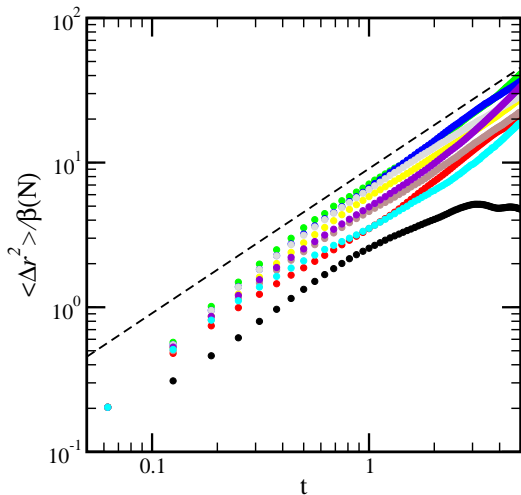


FIG. 9: The mean squared displacements $\langle \Delta r^2 \rangle$ of the beads as a function of time t for various ring length N . The displacements are scaled by a ring length-dependent constant $\beta(N)$ so that all $\langle \Delta r^2 \rangle$ are the same for the shortest experimentally observed time $t = 1/16$ s. The dashed line is proportional to t . The solid

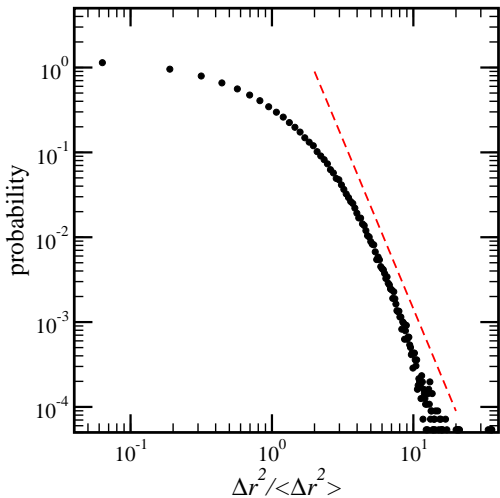


FIG. 10: The probability distribution function for the $\Delta r^2 / \langle \Delta r^2 \rangle$ at $t = 1/16$ s for all ring lengths N . The dashed line has slope -4 .

still behave as if they are randomly (thermally) forced [13, 15]. For shorter times the mean squared displacements increase faster than linearly with time for all but the smallest ring which is consistent with the expected crossover from very short time ballistic motion to long time diffusive dynamics.

For the shortest observation interval of $t = 1/16$ s, we study the distribution of the squared displacements. Since each bead in the ring collides with the plate, on average, once per oscillation, it is highly probable that several beads in the chain will have altered direction due to a collision. Thus, it is unlikely that the $1/16$ s interval

is sufficiently short to deduce an instantaneous velocity. Since the bead-plate collisions occur over a range of phase in the oscillation, however, the beads encounter a range of displacements. Large displacements correspond to collisions and smaller displacements to beads being dragged along by the chain connectedness. In Fig. 10, we plot the probability distribution function of Δr^2 measured at $t = 1/16$ s. The squared displacement is normalized by its mean value. Our data show that small squared displacements are highly probable decaying slowly until $O(\langle \Delta r^2 \rangle)$. For larger displacements the probability decays more rapidly and the large displacement tail decay is consistent with $(\Delta r^2)^{-4}$.

IV. GLOBAL PROPERTIES

Global characteristics of granular rings probe the overall conformation and dynamics of the chain. Below we describe the conformation, roughly speaking, by the chain's size. The size, defined to be the mean radius of gyration, is obtained by averaging over many observations. The global dynamics are described by the motion of the center of mass of the ring.

A. Radius of Gyration

A measure of the global size of a long chain or a polymer is its radius of gyration. Since the chain's configuration is constantly changing owing to collisional excitation with the plate, better measures are the statistical averages of radius of gyration. Given the N position coordinates $\mathbf{r}_i = (x_i, y_i)$ for the beads $i = 1, \dots, N$, we calculate the radius of gyration R_g from

$$R_g^2 = \frac{1}{N} \sum_{i=1}^N (\mathbf{r}_i - \mathbf{r}_{\text{cm}})^2, \quad (7)$$

where $\mathbf{r}_{\text{cm}} = (x_{\text{cm}}, y_{\text{cm}})$ is given by

$$\mathbf{r}_{\text{cm}} = \frac{1}{N} \sum_{i=1}^N \mathbf{r}_i. \quad (8)$$

Since our coordinates are in units of the bead diameter d , the radius of gyration R_g is in these units. We have measured R_g for granular rings for several values of N . Since there are no self-intersections, the ring can be likened to a self avoiding walk that returns to itself.

Averaging over approximately 450 realizations per granular ring of length N , we measure the mean and rms values of R_g . In Fig. 11, we plot $\langle R_g \rangle$ and σ_{R_g} as a function of N for $13 \leq N \leq 309$. In these experiments the lateral boundary has a radius of 53.2 bead diameters. This is an absolute upper bound on $\langle R_g \rangle$ and is shown by the horizontal line in Fig. 11. Our $\langle R_g \rangle$ data for nickel

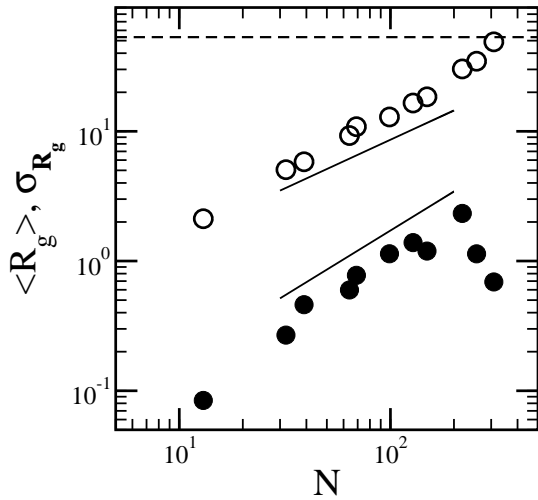


FIG. 11: The mean (\circ) and standard deviation (\bullet) of the radius of gyration vs the length of the rings N . The dashed horizontal line is the radius of the plate. The two solid lines have slopes of $3/4$ (top) and 1 (bottom), respectively.

and brass chains are consistent and increase with N . A power-law fit for the range $20 \leq N \leq 219$ gives an exponent $\nu = 0.85 \pm 0.05$. The σ_{R_g} data in Fig. 11 shows a linear increase with N for $20 \leq N \leq 219$ with a sharp drop for larger N . The sharp drop is associated with the constraining effect of the lateral boundary.

Self avoiding walks have universal scaling characteristics in the large- N limit. In particular, $\langle R_g \rangle \sim N^\nu$ with Flory exponent $\nu = \frac{3}{4}$ in two dimensions [17, 21]. Experiments with surface adsorbed DNA[18], polymer molecular monolayers[19] and connected plastic spheres[20] have measured exponents consistent with the 2D Flory value $\nu = \frac{3}{4}$. Both the DNA and plastic chain had free ends and by being constrained to 2D were self-avoiding. Our measured exponent $\nu = 0.85 \pm 0.05$ is for a ring (likened to self avoiding walk that closes on itself) and is somewhat higher though not inconsistent with these experiments. The σ_{R_g} increase linearly with N in the range $20 \leq N \leq 219$.

B. Center of Mass Motion

Under oscillation the rings sample many configurations with different positions of their center of mass. Since the plate is accurately level, the rings do not drift gravitationally. Any motion of the center of mass is then associated with the overall mobility of the rings. We study the motion of the center of mass of nickel rings with $13 \leq N \leq 309$. The data are acquired at 16 Hz which is sufficiently fast for probing the motion of the ring's center of mass. Given the center of mass \mathbf{r}_{cm} we calculate the magnitude of the average velocity v given by

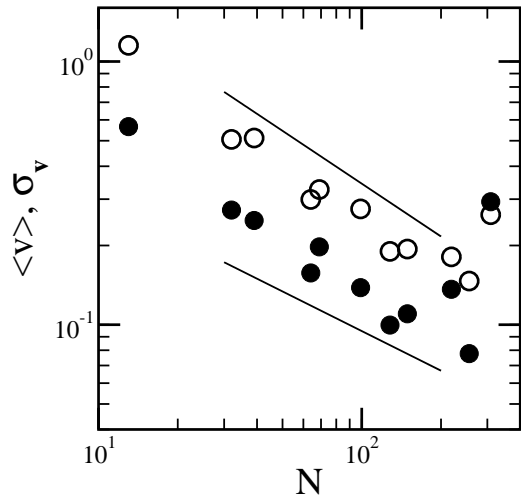


FIG. 12: The mean (\circ) and standard deviation (\bullet) of the center of mass velocity. The straight lines are power-law fits to the data with slopes -0.67 (mean) and -0.59 (standard deviation), respectively.

$$v = \sqrt{\frac{d\mathbf{r}_{cm}}{dt} \cdot \frac{d\mathbf{r}_{cm}}{dt}}. \quad (9)$$

From approximately 400 images per ring we measure the mean and rms values of v . In Fig. 12, we plot the mean $\langle v \rangle$ and standard deviation σ_v for several N . For our largest ring $N = 309$ significant interaction with the lateral boundary appears to be responsible for the unexpectedly large $\langle v \rangle$ and σ_v . Assuming scaling relations $\langle v \rangle \sim N^\eta$ and $\sigma_v \sim N^\zeta$ power-law fits for $13 \leq N \leq 256$ give $\eta = -0.67 \pm 0.08$ and $\zeta = -0.59 \pm 0.14$. The speed v varies from just over 1 bead diameter/s for $N = 13$ to about 1/10 bead diameters/s for $N = 256$. As N increases more and more segments of the ring move independently resulting in large cancellations to contributions to center of mass motion. Qualitatively, this diminished mobility with increasing chain length resembles the behavior observed for a random polymer where the diffusivity is inversely proportional to the molecular weight [21].

As with the bead displacements studied in Section III D, we can study the dynamics of the ring center of mass. The squared displacement that ring center-of-mass undergoes between time τ and $\tau + t$ is $\Delta R_{cm}^2(t, \tau, N) = (\mathbf{r}_{cm}(\tau + \mathbf{t}) - \mathbf{r}_{cm}(\tau)) \cdot (\mathbf{r}_{cm}(\tau + \mathbf{t}) - \mathbf{r}_{cm}(\tau))$. For the data, the times τ and t are chosen to coincide with the image acquisitions, *i.e.*, multiples of $1/16$ s and the displacement is measured in units of the bead diameter. Averaging over all possible values of τ we define the mean squared ring center of mass displacement:

$$\langle \Delta R_{cm}^2 \rangle(t, N) = \langle \Delta R_{cm}^2(t, \tau, N) \rangle_\tau. \quad (10)$$

The time dependence of $\langle \Delta R_{cm}^2 \rangle$ is plotted in Fig. 13. Here, we have assumed a length dependent constant factor $\alpha(N)$ such that the mean squared displacements are

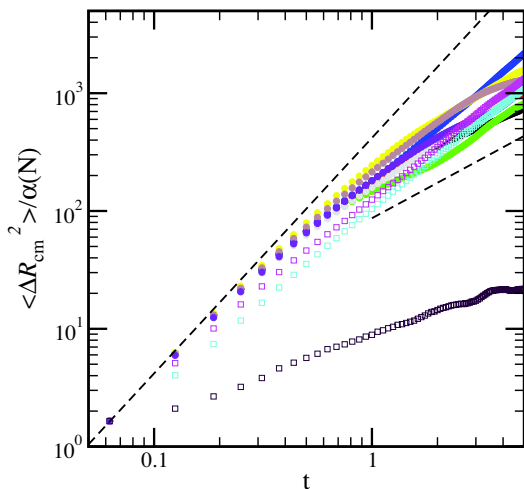


FIG. 13: The mean squared displacements $\langle \Delta R_{cm}^2 \rangle$ of the ring center of mass as a function of time t for various ring length N . The displacements are scaled by an ring length-dependent constant $\alpha(N)$ so that all $\langle \Delta R_{cm}^2 \rangle$ are the same for the shortest experimentally observed time $t = 1/16$ s. The dashed lines are proportional to t and t^2 . The $\langle \Delta R_{cm}^2 \rangle$ from the three longest rings $N = 219, 256$ and 309 are shown in magenta, cyan and maroon open square symbols respectively.

the same for the shortest experimentally observed time $t = 1/16$ s.

For times corresponding to less than about 10 plate oscillations, the $\langle \Delta R_{cm}^2 \rangle / \alpha(N)$ increase quadratically with time for all rings except the three largest rings with $N = 219, 256$ and 309 . The constraining effect of the plate's lateral boundary explains the less than quadratic time dependence of $\langle \Delta R_{cm}^2 \rangle / \alpha(N)$ for large rings. For times in excess of about 10 plate oscillations, the $\langle \Delta R_{cm}^2 \rangle / \alpha(N)$ approaches a linear increase with time. The short time behaviour is consistent with ballistic motion of the ring center of mass. This suggests that at short times the motion of the ring center of mass is dominated by coherent large bead displacements. The longer time behaviour averages over several, apparently random, large displacements resulting in the approach to diffusive motion.

The distribution of the squared displacements of the ring center of mass is studied for the shortest observation interval of $t = 1/16$ s. At this time scale the center of mass motion is ballistic and so an average velocity proportional to the displacement may be inferred. In Fig. 14, we plot the probability distribution function of ΔR_{cm}^2 measured at $t = 1/16$ s. The squared displacement is normalized by its mean value. Our data show that small squared displacements are highly probable with the probability decaying consistent with $(\Delta R_{cm}^2)^{-1.5}$. The small squared displacements of the ring center of mass arise from averaging the almost independent motions of the beads on the ring. The less probable large squared displacements occur from rarer coherent motions of segments of beads on the rings.

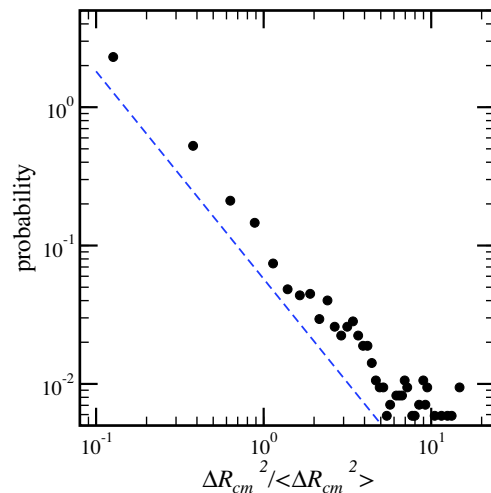


FIG. 14: The probability distribution function for the $\Delta R_{CM}^2 / \langle \Delta R_{CM}^2 \rangle$ at $t = 1/16$ s for all ring lengths N . The dashed line has slope -1.5 .

V. CONCLUSION

In this paper we presented an experimental study of vibrated granular rings. Our study elucidates the statistical characterization of various local and global properties. We have been particularly interested in power-law scaling of average properties with the chain size. Local properties were on the scale of a bead. We specifically studied the inter-bead separations, angles, shape and positional dynamics. Global or macroscopic properties were on the scale of the entire chain. In particular our study probed the size and overall motion of vibrated rings.

The size of various parts of the experimental apparatus limits our study to chains of moderate bead numbers typically $N < 300$ for rings. Consequently the rings are analogous to relatively short self-avoiding walks. Despite the relatively short chain lengths, we are still able to deduce reasonable scaling laws. The mean global properties typically show power-law scaling over the modest range in N with cross-over effects at small N and pronounced finite-size effects at large N . Generally in between the extremes, power-law scaling appears to provide an adequate description.

The system of vibrating granular chains presents a fertile ground for experimentally studying nonequilibrium statistical mechanics. It is particularly well-suited since it permits simultaneous measurements of micro- and macroscopic variables. Our future experiments will primarily concern this aspect in the setting of multi-chain experiments. We expect to study groups of rings and free-end chains and measure the average individual and collective properties as they vary with density and conformation. The variation of the average individual or microscopic properties with the macroscopic density will elucidate the statistical mechanics of this system. Rings of different N have different internal degrees of freedom.

A tight ring with $N = 8$ is almost circular and has small deviations from this configuration under vibrational excitation. Its space of configurations is small and we may think of it as having almost zero internal degrees of freedom. Rings of larger N , however, have shapes that depart significantly from simple conformations and consequently a large configuration space and thus many internal degrees of freedom. The richness bestowed by the ability to vary these internal degrees of freedom will permit the detailed study of their bearing on macroscopic

properties of a collection of such rings. Other cooperative behavior arising from rings of different sizes, a collection free-end chains and self-interactions between different regions of very long chains afford abundant possibilities for studying nonequilibrium statistical physics.

We thank Mike Rivera and Brent Daniel for useful suggestions regarding the experiment and Matt Hastings. This research is supported by the U.S. DOE (W-7405-ENG-3

-
- [1] L.P. Kadanoff, *Rev. Mod. Phys.*, **71**, 435 (1999).
 - [2] P.G. de Gennes, *Rev. Mod. Phys.*, **71**, S374 (1999).
 - [3] H.M. Jaeger, S.R. Nagel, and R.P. Behringer, *Rev. Mod. Phys.*, **68**, 1259 (1996).
 - [4] B. Umbanhowar, F. Melo, and H.L. Swinney, *Nature (London)* **382**, 793 (1996).
 - [5] J.R. de Bruyn, C. Bizon, M.D. Shattuck, D. Goldman, J.B. Swift, and H.L. Swinney, *Phys. Rev. Lett.*, **81**, 1421 (1998).
 - [6] J.R. de Bruyn, B. Lewis, M.D. Shattuck, and H.L. Swinney, *Phys. Rev. E.*, **63**, 041305 (2001).
 - [7] A. Kudrolli, M. Wolpert, and J.P. Gollub, *Phys. Rev. Lett.*, **78**, 1383 (1997).
 - [8] J.S. Olafsen and J.S. Urbach, *Phys. Rev. Lett.*, **81**, 4369 (1998).
 - [9] J.B. Knight, C.G. Fandrich, Chun-Ning Lau, H.M. Jaeger, and S.R. Nagel, *Phys. Rev. E.*, **51**, 3957 (1995).
 - [10] E.R. Nowak, J.B. Knight, E. Ben-Naim, H.M. Jaeger, and S.R. Nagel, *Phys. Rev. E.*, **57**, 1971 (1998).
 - [11] J.S. Olafsen and J.S. Urbach, *Phys. Rev. E.*, **60**, R2468 (1999).
 - [12] F. Rouyer and N. Menon, *Phys. Rev. Lett.*, **85**, 3676 (2000).
 - [13] E. Ben-Naim, Z.A. Daya, P. Vorobieff, and R.E. Ecke, *Phys. Rev. Lett.*, **86**, 1414 (2001).
 - [14] A. Belmonte, M.J. Shelley, S.T. Eldakar, and C.H. Wiggins, *Phys. Rev. Lett.*, **87** 114301 (2001).
 - [15] M.B. Hastings, Z.A. Daya, E. Ben-Naim, and R.E. Ecke, *Phys. Rev. E.*, **66**, 025102(R) (2002).
 - [16] R. E. Ecke, Z. A. Daya, M. K. Rivera, and E. Ben-Naim, *Materials Research Society Symposium Proceedings*, **759**, 129 (2003).
 - [17] P. G. de Gennes, *Scaling Concepts in Polymer Physics*, (Cornell, Ithaca, 1979).
 - [18] B. Maier and J.O. Rädler, *Phys. Rev. Lett.*, **82**, 1911 (1999).
 - [19] R. Villanove and F. Rondelez, *Phys. Rev. Lett.*, **45**, 1502 (1980).
 - [20] J.J. Prentis and D.R. Sisan, *Phys. Rev. E.*, **65**, 031306 (2002).
 - [21] M. Doi and S. F. Edwards, *The Theory of Polymer Dynamics*, (Clarendon Press, Oxford, 1986).